Sustainable Energy & Fuels

ROYAL SOCIETY OF CHEMISTRY

PAPER

View Article Online
View Journal | View Issue

Check for updates

Cite this: *Sustainable Energy Fuels*, 2025, **9**, 2961

Immobilisation of a molecular iridium complex on periodic mesoporous organosilica for heterogeneous water oxidation catalysis†

Raúl Rojas-Luna, *[ab] Juan Amaro-Gahete, [bc] Sumit Konar, [a] Francisco J. Romero-Salguero, [b] Dolores Esquivel *[b] and Souvik Roy *[a]

Received 11th March 2025
Accepted 21st April 2025

DOI: 10.1039/d5se00371g

rsc.li/sustainable-energy

Water oxidation (WO) is considered the main bottleneck of artificial photosynthesis. In this scenario, the development of efficient water oxidation catalysts (WOCs) is essential for optimising artificial solar energy conversion systems. Herein, we report the synthesis and characterisation of a new Ir-based molecular catalyst by coordinating IrCp*Cl (Cp* = pentamethylcyclopentadienyl) to a N-chelating heterocyclic ligand, 3,6-dipyridin-2-ylpyridazine (dppz). Kinetics and water oxidation catalytic activity for the half-sandwiched iridium(III) pre-catalyst have been evaluated by using cerium ammonium nitrate (CAN) as an electron acceptor. Heterogenisation of the molecular Ir complex on a previously reported dppz-functionalised PMO (NdppzPMO) was demonstrated to synthesize a robust and recyclable solid catalyst (Ir-PMO) with well-defined catalytic sites. This approach stabilises the molecular active site during catalysis by preventing the diffusion-controlled deactivation pathways observed in the homogeneous phase. In the presence of CAN, Ir-PMO exhibits a steady evolution of oxygen over multiple catalytic cycles, producing a total amount of 1349 μmol O_2 (TON_{Ir} = 1874) until the system starts to deactivate due to the deposition of cerium oxide (CeO_2) nanoparticles. The hydrophobic nature of Ir-PMO facilitates diffusion of the oxidising agent towards the catalytic sites, leading to a faster catalytic rate compared to an analogous silica-based material with a covalently attached Ir-complex.

1. Introduction

The conversion of water into molecular oxygen and hydrogen represents a fundamental process in artificial photosynthesis, functioning as a critical mechanism for solar fuel production.[1] This reaction can be delineated into two principal half-reactions (eqn (1) and (2)):

$$2H_2O \rightarrow O_2 + 4H^+ + 4e^- \quad (1)$$

$$4H^+ + 4e^- \rightarrow 2H_2 \quad (2)$$

Effectively coupling these half-reactions poses substantial challenges, particularly with regard to the water oxidation step occurring in photosystem II of natural photosynthesis, which necessitates the intricate transfer of four electrons.[2] The elevated energy barrier associated with this transformation renders it one of the most challenging processes in water splitting, underscoring the necessity for robust catalysts to facilitate the reaction. Addressing the thermodynamic and kinetic drawbacks inherent to this step has prompted extensive research into water oxidation catalysts (WOCs).[3,4]

In this context, the Mn_4CaO_5 core of photosystem II has emerged as a model for understanding the structure and mechanisms of multimetallic complexes. It is widely accepted that multinuclear metal centres are particularly effective as WOCs due to their ability to distribute oxidising equivalents and stabilise reactive intermediates. Various catalytic systems have been developed, including molecular complexes based on tetramanganese, dimanganese, and diruthenium, as well as heterogeneous catalysts utilising nanostructured metal oxides such as manganese, cobalt, iron, ruthenium, and iridium.[5,6]

[a]*Department of Chemistry, School of Natural Sciences, University of Lincoln, Green Lane, Lincoln, Lincolnshire, LN6 7DL, UK. E-mail: rrojas-luna@lincoln.ac.uk; sroy@lincoln.ac.uk*

[b]*Departamento de Química Orgánica, Instituto Químico para la Energía y el Medioambiente (IQUEMA), Facultad de Ciencias, Universidad de Córdoba, Campus de Rabanales, Edificio Marie Curie, E-14071 Córdoba, Spain. E-mail: q12esmem@uco.es*

[c]*UGR-Carbon – Materiales Polifuncionales Basados en Carbono, Departamento de Química Inorgánica, Unidad de Excelencia Química Aplicada a Biomedicina y Medioambiente, Universidad de Granada, ES18071 Granada, Spain*

† Electronic supplementary information (ESI) available: Further experimental method details, characterisation and cerium-driven water oxidation of [IrCp*Cl(dppz)]Cl (Fig. S1–S11, S17, S26 and S27), additional characterisation and catalytic activity data of Ir-PMO pre- and post-catalysis (Fig. S12–S16 and S18–S20), cerium-driven water oxidation of Ir-SBA and comparison of catalytic activity between Ir-SBA and Ir-PMO (Fig. S23–S25), and supporting tables (Tables S1–S8). CCDC 2404149. For ESI and crystallographic data in CIF or other electronic format see DOI: https://doi.org/10.1039/d5se00371g

Recent studies have also emphasised the potential of single metal site catalysts for water oxidation, including noble metals like ruthenium and iridium, alongside earth-abundant alternatives such as iron and cobalt.[7] Single-site WOCs offer several advantages, including improved atom economy, simpler synthesis and characterisation, mechanistic investigations, and the ability to systematically tune their geometric and electronic structures. This focus on single-site catalysts paves the way for creating innovative molecular assemblies that integrate catalytic functionalities with other desirable properties such as recyclability, robustness, and longevity.[8]

Particularly, iridium-based complexes have garnered considerable attention due to their superior catalytic activity and stability under the harsh oxidative conditions required for water oxidation.[9–13] Early studies by Crabtree and co-workers demonstrated the efficiency of homogeneous iridium complexes, especially those featuring pentamethylcyclopentadienyl (Cp*) ligands, which provide a robust platform for stabilising high-valent iridium intermediates necessary for the catalytic cycle.[14,15] However, despite their high activity, homogeneous iridium catalysts face limitations related to recyclability and long-term stability.[16] This has prompted a shift toward the development of heterogeneous systems, where the iridium catalyst is immobilised on a solid support, offering advantages in terms of reusability and ease of separation.[17]

Various supports have been explored for this purpose, including metal–organic frameworks (MOFs), layered double hydroxides (LDHs), carbon-based supports, and mesoporous silicas.[18,19] MOFs, in particular, have gained considerable attention due to their highly ordered porous structures and tunable chemical environments, which make them promising candidates for immobilising metal complexes such as iridium-based WOCs.[20] In 2011, Lin *et al.* pioneered the successful immobilisation of iridium complexes on a MOF support, achieving moderate catalytic performance in water oxidation reactions.[21] The iridium complexes were anchored to the bipyridine sites of the MOF, which served as coordination points for the metal centre, thus providing a heterogeneous catalytic system. However, diffusion limitations due to their relatively small pore sizes (typically in the range of 0.5–1 nm) and oxidative degradation of Cp* have been a significant drawback. These narrow channels can hinder the efficient transport of reactants and products, leading to reduced catalytic activity over time, particularly in larger-scale applications where diffusion becomes a critical factor. Moreover, the stability of MOFs under the harsh oxidative and acidic conditions required for water oxidation remains a concern, as many MOFs are prone to degradation or structural collapse under these conditions.[22]

In response to these challenges, other porous materials such as mesoporous silicas have been considered as alternative supports for iridium catalysts.[23] Specifically, periodic mesoporous organosilicas (PMOs), which are a class of hybrid materials characterised by tuneable pore sizes ranging from 2 to 50 nm and high surface areas, offering enhanced accessibility to active sites, have emerged as ideal supports for heterogeneous catalysis due to their ability to incorporate organic functionalities within their framework.[24] In this context, bipyridine-functionalised PMOs have been shown to provide a stable and effective support for the immobilisation of iridium complexes. In 2016, Inagaki *et al.* reported the use of bipyridine-bridged PMOs as supports for iridium catalysts, achieving enhanced catalytic activity in the oxidation of water, primarily due to the increased stability of the catalyst and the improved diffusion of reactants through the mesoporous structure.[25]

In this work, we report for the first time the synthesis, crystal structure, electrochemical characterisation, and cerium ammonium nitrate (CAN) driven water oxidation catalytic activity of a half-sandwich iridium(III) complex coordinated to a dppz ligand. The bidentate nature and electron-deficient pyridazine ring of the dppz ligand render the unexplored [IrCp*Cl(dppz)]Cl complex an interesting system to study for the water oxidation reaction under homogeneous and heterogeneous conditions and benchmark its activity against known iridium catalysts. Investigation of the molecular complex in solution can provide key mechanistic insights towards understanding the catalytic properties of solid materials with a heterogenised Ir-complex. Herein, we introduce a facile synthetic strategy for immobilisation of the $[IrCp^*Cl(dppz)]^+$ complex on periodic mesoporous organosilicas (PMOs) to synthesize an efficient heterogeneous WOC, following our previously reported methodology.[26] To our knowledge, this is the first study that delves into the use of dppz-functionalised PMO-supported iridium complex for the oxygen evolution reaction, and the results indicate significant improvements in both catalytic performance and stability compared to the homogeneous system. These findings open new avenues for the design of highly efficient heterogeneous catalysts for artificial photosynthesis and other energy conversion processes.

2. Results and discussion

The half-sandwich Ir^{III} catalyst, [IrCp*Cl(dppz)]Cl, was synthesised by a reaction of 1 equiv. of $[IrCp^*Cl_2]_2$ dimer with 1 equiv. of the neutral ligand dipyridylpyridazine (Fig. 1a). The X-ray crystal structure is shown in Fig. 1b, and the crystallographic data are summarised in Tables S1–S3.† The iridium centre displays a characteristic three-legged piano stool geometry as expected for a half-sandwich complex. The Cp* ring binds in an η^5 mode, and the dppz ligand coordinates in a bidentate fashion. A chloride ligand occupies the third coordination site. The two uncoordinated pyridinic N atoms of the dppz ligand are positioned *trans* to each other to minimise the electrostatic repulsion. The Ir–N bond lengths (2.097 and 2.090 Å) are consistent with those reported for an analogous bipyridine complex.[27] The powder X-ray pattern of the complex closely matched the simulated pattern, confirming the crystalline nature of the synthesised complex (Fig. S1†). The stability of the iridium complex was evaluated using optical spectroscopy. Monitoring of the UV-vis spectrum in organic solvent over 2 h exhibited unaltered patterns, confirming the stability of the complex in organic media (Fig. S2a†).[28] However, significant changes were observed at 370 nm in acidic aqueous solution (Fig. S2b†) due to exchange of the chloride ligand with an aquo ligand to form $[IrCp^*(OH_2)(dppz)]^{2+}$ species.[29] The lability of the

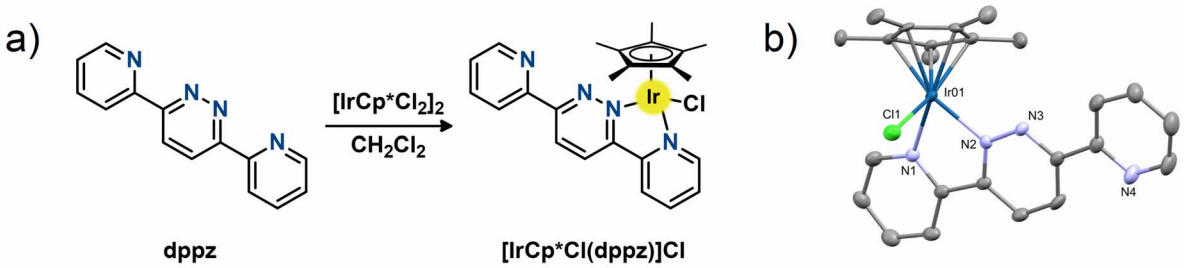

Fig. 1 (a) Synthesis of the half-sandwich [IrCp*Cl(dppz)]Cl complex. (b) Molecular structure of [IrCp*Cl(dppz)]Cl determined by single-crystal X-ray diffraction (hydrogen atoms and counter ions are omitted for clarity).

chloride ligand in aqueous solution was further confirmed by high-resolution mass spectrometry (HRMS) (Fig. S3†).

The synthesised iridium complex was evaluated as a potential homogeneous catalyst for CAN-driven water oxidation under acidic aqueous conditions. Aqueous solutions were acidified with nitric acid due to faster rates that have been reported in comparison with other acids commonly employed, such as triflic acid,[30,31] while CAN was employed as a sacrificial one-electron oxidant since it is unable to independently catalyse the formation of dioxygen.[32] For this purpose, O_2 evolution was monitored by differential pressure manometry, while depletion of CAN was monitored by *in situ* UV-vis spectroscopy at a fixed wavelength of 390 nm, where the iridium complex shows minimal absorption after Cl^- ligand exchange (*vide infra*). Water oxidation reactions were conducted at different ratios between the electron acceptor and the catalyst ([CAN] : [Ir] = 100, 400 and 1000) (Fig. S4 and Table S4†). Although the decay of the oxidant is clearly accompanied by the generation of dioxygen, the activity is notably influenced by the [CAN] : [Ir] ratio. At [CAN] : [Ir] = 100, the catalytic system exhibited slower oxygen evolution rates (TOF_{Ir} = 1.20 min^{-1}) over the initial 15 min compared to the rate of CAN depletion (TOF_{Ce} = 2.50 min^{-1}). The turnover frequency for Ce^{IV} depletion (TOF_{Ce}) is defined as the ratio of the number of oxidising equivalents consumed, divided by four, and the moles of the catalyst, since one catalytic cycle requires the consumption of 4 moles of Ce^{IV}. This is consistent with previous reports on an analogous [IrCp*Cl(bpy)]Cl complex that demonstrated faster CAN consumption than O_2 evolution at relatively low [CAN] : [Ir] ratios (80–320 equiv. CAN).[33] As the [CAN] : [Ir] ratio increased, the rates of O_2 evolution and CAN depletion tended to equilibrate with TOF values of 2.41 and 2.94 min^{-1} at [CAN] : [Ir] = 1000, respectively. Interestingly, both kinetics converged at approximately halfway through the catalytic turnovers (TON_{Ir} = 118), indicating similar rates through the course of the reaction (Fig. S4c†). The yield of O_2 also increased from ~60% at [CAN] : [Ir] = 100 to ~82% at [CAN] : [Ir] = 1000. This hints at a potential oxidative activation of the iridium complex that requires the consumption of CAN (*vide infra*). The plateauing of the oxygen evolution was attributed to the complete consumption of CAN. The catalysis could indeed be restarted by addition of fresh CAN, albeit with slightly lower O_2 yield and TON_{Ir} in the second cycle (Table 1 and Fig. S17†). This confirms that the molecular integrity of the iridium complex was largely maintained. The molecular nature of the homogeneous catalysis was further confirmed by DLS, which showed no evidence of IrO_2 nanoparticles in the post-catalysis mixture. The TOF for O_2 evolution and the yield of O_2 exhibited by [IrCp*Cl(dppz)]Cl at pH 1 are comparable to those reported for an analogous 2,2′-bipyridine complex (Table S5†). However, the rate of O_2 evolution is slower compared to IrCp*-based WOCs with more electron donating bidentate ligands.[33,34] We hypothesise that the electron withdrawing nature of the uncoordinated pyridine renders the central pyridazine ring of dppz electron deficient. The lower donating capability of dppz provides limited stabilisation to the high-valent iridium-oxo intermediate, leading to slower catalysis.

For an in-depth investigation of the kinetics of water oxidation, concentration-dependent experiments were conducted. Initial rates were calculated by linear regression during the first 60 seconds of the reaction. At a constant Ir catalyst concentration (10 μM), a fractional order of 0.83 in the oxidant was determined from the slope of the corresponding double logarithmic plot (Fig. S5a–c†). However, zero-order kinetics was found with 10 mM CAN (Fig. S6†). A similar finding was also reported by Crabtree *et al.*[35] for an analogous [IrCp*Cl(bpy)]Cl complex, which displayed kinetics lower than first-order (0.73) at low oxidant equivalents and zero-order at higher equivalents, whereas the $[IrCp^*(OH)_2]^{2+}$ catalyst showed zero-order kinetics. This behaviour emphasises a clear dependence of the rate-determining step on the concentration of the sacrificial oxidant, controlled by the generation of high-valent metal-oxo species at low oxidant concentrations and by O–O bond formation at higher concentrations.[35] Analogously, the kinetics of Ce^{IV} depletion was determined to be first order in the catalyst (Fig. S5d–f†). Therefore, under these conditions, the rate law for Ce^{IV} depletion is defined as $r = k[Ir][Ce^{IV}]^{0.83}$.

For a better understanding of the nature of the active species engaged in catalysis, the spectral changes for $[IrCp^*Cl(dppz)]^+$ were monitored. The addition of CAN (2 μmol, 100 equiv.) into a solution of $[IrCp^*Cl(dppz)]^+$ (10 μM, HNO_3 0.1 M, pH = 1.0) led to the appearance of a new band at 600 nm (Fig. S7†), which

Table 1 Catalytic activity of Ir-PMO and homogeneous [IrCp*Cl(dppz)]Cl towards water oxidation in the presence of CAN

Catalyst	Reaction cycle	O_2 evolution (μmol O_2)	O_2 yield[a] (%)	TON	TOF[b] (min^{-1})
Ir-PMO	1st	210	84	292	0.59
	2nd	220	88	306	1.00
	3rd	228	91	317	1.09
	4th	235	94	326	1.04
	5th	235	94	326	0.50
	6th	221	89	307	0.25
[IrCp*Cl(dppz)]Cl	1st	227	91	315	2.36
	2nd	199	80	276	1.09

[a] Calculated in relation to the theoretical maximum amount of 250 μmol oxygen evolved. [b] Calculated in the first 15 min after the addition of the oxidising agent. Experimental conditions: 100 mM CAN in HNO_3 (10 mL, 0.1 M, pH = 1) using 0.72 μmol Ir catalyst.

is also characteristic of other half-sandwiched iridium complexes with bidentate ligands.[32] The absorbance increased during CAN depletion and plateaued after ~40 min when the solution bleached and the formation of oxygen bubbles ceased. The addition of ethanol (50 μL) gradually quenched this band, which nearly disappeared after 15 minutes. Since ethanol cannot reduce iridium oxide nanoparticles,[36,37] we attribute the new absorption at 600 nm to high valent iridium species formed during catalysis, which is consistent with the molecular nature of the water oxidation reaction as indicated by the DLS results.[38] Notably, the reaction solution turned blue after Ce^{IV} depletion (Fig. S17 inset†), indicating the formation of high-valent iridium species during catalysis. The absence of IrO_2 nanoparticles in the reaction mixture is also in line with previous reports on IrCp* complexes bearing bidentate chelating ligands such as 2,2′-bipyridine, 2-phenylpyridine, and 2-(2′-pyridyl)-2-propanoate,[38–41] as well as monodentate N-heterocyclic carbene with pendant hydroxy groups.[42] Here, dppz serves as an *N*,*N*′-bidentate ligand to form a robust IrCp* complex and provides a suitable coordination environment for the stabilisation of high valent iridium species, similar to the aforementioned ligands.

The redox behaviour of [IrCp*Cl(dppz)]Cl was examined by cyclic voltammetry (CV) and differential pulse voltammetry (DPV) in aqueous and non-aqueous (acetonitrile) electrolytes under nitrogen. As previously mentioned, the iridium complex predominantly exists as $[IrCp^*(OH_2)(dppz)]^{2+}$ under aqueous conditions. Cyclic voltammograms recorded for [IrCp*Cl(dppz)]Cl at different pH are shown in Fig. 2a. The cyclic voltammogram at pH 1 showed the onset of an oxidation wave at ~1.66 V *vs.* RHE ascribed to electrocatalytic water oxidation. This indicates that CAN-driven water oxidation by [IrCp*Cl(dppz)]Cl is

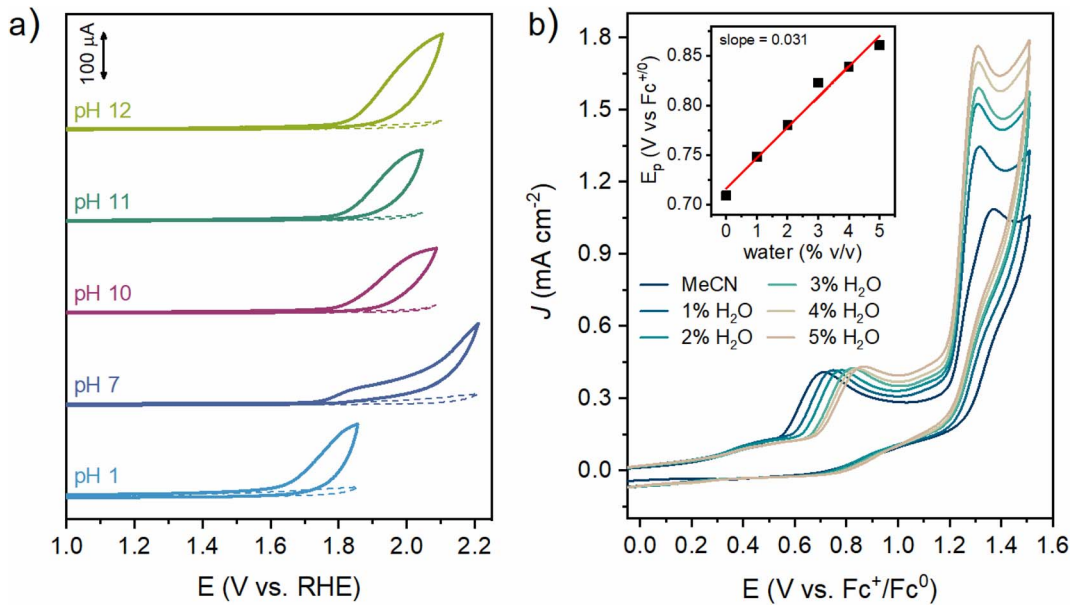

Fig. 2 (a) pH-dependent cyclic voltammograms of [IrCp*Cl(dppz)]Cl (1 mM) in aqueous solution. The dashed lines show the blank CVs in the absence of a catalyst. Conditions: glassy carbon working electrode, Ag/AgCl/KCl (3 M) reference electrode, Pt wire counter electrode, 0.1 M electrolyte, and a scan rate of 100 mV s^{-1}. (b) Cyclic voltammograms of [IrCp*Cl(dppz)]Cl (1.0 mM) in neat MeCN and with increasing water content (1–5%). Inset shows the linear fit of the shift of the peak potential for the first oxidation step against the concentration of water. Conditions: glassy carbon working electrode, Pt wire counter electrode, Ag/$AgNO_3$ (10 mM) reference electrode, and $TBABF_4$ (0.1 M) supporting electrolyte.

thermodynamically feasible since the standard redox potential of the Ce^{IV}/Ce^{III} couple is reported as 1.7 *vs.* RHE at pH = 1, which can rise to over 1.81 V *vs.* RHE at high Ce^{IV} concentrations.[32] At neutral pH, the CV exhibited an irreversible oxidation wave at ~1.82 V *vs.* RHE (~1.4 V *vs.* NHE), which overlapped with the onset of the subsequent electrocatalytic water oxidation wave. This oxidation step was further confirmed by DPV experiments (Fig. S8†), which can be tentatively assigned to an Ir^{IV}/Ir^{III} redox couple.[43,44] The absence of this oxidation wave at acidic pH could be related to the protonation of uncoordinated pyridinic or pyridazinic nitrogens, which can anodically shift the oxidation wave. This would have lowered the donating capability of the dppz ligand, leading to a more electron deficient Ir centre that undergoes oxidation at a higher potential. Alternatively, pH-dependent speciation of the $[IrCp^*(OH_2)(dppz)]^{2+}$ involving deprotonation of the coordinated water ligand is also a possibility. At pH 12, a prominent catalytic wave for water oxidation was observed at ~1.87 V (*vs.* RHE), which is consistent with previous reports.[45] The onset of the catalytic water oxidation reaction displayed a near-Nernstian dependence on the solution pH (~62 mV pH^{-1}) in the pH range of 7–12 (Fig. S9†).

The CV of [IrCp*Cl(dppz)]Cl in acetonitrile (Fig. S10a†) displayed a partially reversible oxidation peak at 0.64 V (*vs.* $Fc^{+/0}$), consistent with an EC process (an electron transfer, E, followed by a chemical reaction, C), in which the oxidation is followed by a chemical step. Based on previous reports on an analogous $[IrCp^*Cl(bpy)]^+$ complex, this peak can be attributed to oxidation of the metal-bound pentamethylcyclopentadienyl.[45,46] The lack of reversibility of the CV response could be caused by chemical deprotonation of the Cp* methyl group(s) following the electron transfer. Over ten successive CV scans (Fig. S10a inset†), the oxidation peak displayed a gradual shift to 0.74 V, suggesting that partial oxidation rendered Cp* harder to oxidise. The return scan showed a much-shifted reduction wave at 0.35 V with a smaller peak current. Interestingly, this oxidation process was not observed in the voltammograms recorded under aqueous conditions. The formation of deposits on the electrode surface was excluded by performing scan rate dependent CVs, which confirmed that the oxidative and reductive peaks remained diffusion controlled (Fig. S10b–d†). Upon extending the scanning window to more oxidising potential (1.5 V *vs.* $Fc^{+/0}$), a second irreversible oxidation wave was observed at 1.4 V and the reduction wave at 0.35 V disappeared during the return scan (Fig. 2b, S10c and d†). This oxidation is assigned to the Ir^{IV}/Ir^{III} couple, which promotes the water oxidation reaction. The reductive scan (Fig. S11†) of [IrCp*Cl(dppz)]Cl displayed an irreversible reduction at −1.20 V, which has been reported to be a two-electron reductive elimination step ($d^6 \rightarrow d^8$) with clearly separated cathodic and anodic peaks ($\Delta E_p \sim 0.23$ V).[46] The tentative mechanism can be described as an ECE process that involves a metal centred reduction, followed by rapid loss of Cl^-, and then a second reduction step that requires less energy than the first.

To confirm the origin of the water oxidation activity of [IrCp*Cl(dppz)]Cl, CVs were recorded in acetonitrile in the presence of water (1–5%, v/v). As shown in Fig. 2b, incremental addition of water led to an increase of peak current in the second oxidation process, leading to a catalytic water oxidation peak at 1.30 V. This observation suggests that metal centred oxidation of Ir^{III} to Ir^{IV} initiates the water oxidation reaction. Interestingly, the first oxidation peak underwent an incremental shift to a more positive potential as more water was added to the system and the peak potential shift exhibited a linear correlation with the water content (Fig. 2b, inset). We speculate that this shift is caused by the incremental displacement of inner-sphere chloride ligands with aquo ligands when water is present in the organic phase.[47,48]

Encouraged by the promising water oxidation performance of the iridium catalyst, we targeted immobilisation of IrCp*Cl units onto a periodic mesoporous silica scaffold functionalised with dipyridylpyridazine ligands (NdppzPMO) to synthesize a hybrid solid catalyst (Ir-PMO).[26] The synthetic procedure of the heterogeneous Ir-PMO WOC is depicted in Scheme 1. Post-synthetic metalation of the chelating dppz motifs of NdppzPMO with $[IrCp^*Cl]_2$ resulted in the formation of isolated [IrCp*Cl(dppz)]Cl sites in Ir-PMO and a concomitant colour change from pink to pale orange. The iridium content was estimated by ICP-MS to be 0.24 mmol g^{-1} when $[IrCp^*Cl]_2$ was added in a 1 : 1 Ir/dppz molar ratio, leading to ~60% of coordinated dppz units. Interestingly, the loading of iridium remained largely unchanged even when a higher amount of $[IrCp^*Cl]_2$ (*i.e.*, 1.5 or 2 Ir/dppz molar ratio) was used for the metalation reaction (Table S6†), suggesting limited accessibility to the deeply embedded dppz sites within the PMO mesopores.

Consistent with our previous reports,[26,49] the low-angle powder X-ray diffraction (PXRD) pattern of NdppzPMO exhibited an intense reflection plane at *ca.* 1.9° ($d_{100} = 4.6$ nm) as well as two broad reflection planes at higher incidence angles of *ca.* 3.3° and 3.8°, characteristic of an ordered mesoporous structure. The PXRD pattern of Ir-PMO confirmed the preservation of the two-dimensional hexagonal lattice of the starting material (Fig. 3a) upon immobilisation of the iridium complex. However, the metalation process was accompanied by a significant reduction in the intensity of the diffractions, even leading to the disappearance of the reflection planes at higher incidence angles (Fig. 3a, inset), which suggested differences in the scattering contrasts within the pores. The integrity of the ordered mesoporous structure was also confirmed by transmission electron microscopy (Fig. S12†). The elemental distribution was investigated by energy-dispersive X-ray spectroscopy (EDS) elemental mapping (Fig. S13†), where Ir species were evenly distributed throughout the sample. Nitrogen physisorption experiments revealed type IV isotherms (Fig. 3b), typical of ordered mesoporous materials. The textural properties of Ir-PMO decreased as a result of complexation on the inner pore surface (Table S7†), leading to surface area (S_{BET}), pore volume (P_V) and pore diameter (D_P) values of 612 m^2 g^{-1}, 0.40 cm^3 g^{-1} and 2.7 nm, respectively.

The formation of heterogenised [IrCp*Cl(dppz)]Cl complexes was studied by Fourier transform infrared spectroscopy (FT-IR), UV-vis diffuse reflectance spectroscopy (UV-vis DRS), solid-state ^{13}C cross polarisation magic-angle spinning (CP/MAS) NMR and X-ray photoelectron spectroscopy (XPS). FT-

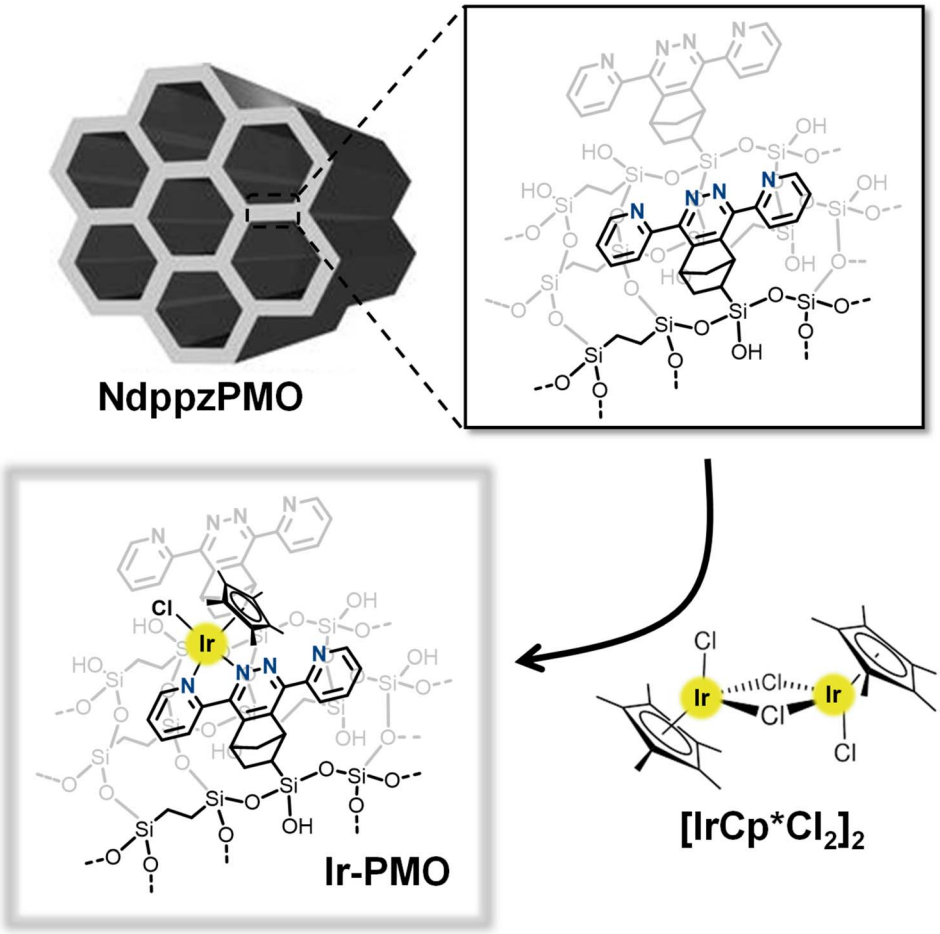

Scheme 1 Synthesis of Ir-PMO.

IR spectra of the homogeneous and heterogeneous [IrCp*Cl(dppz)]Cl complexes are shown in Fig. 3c. The homogeneous complex exhibited a combination of the characteristic C=N and C=C skeletal vibrations of the N-heterocyclic ligand in the range of 1400–1600 cm^{-1}, along with representative Cp* vibrations. Interestingly, the formation of the Ir complex led to the appearance of two vibrational modes shifted towards higher frequencies (1610 and 1652 cm^{-1}), which evidence different environments for the pyridazine/pyridine heterocycles compared to the uncoordinated dppz ligand.[50] Furthermore, the new signal observed at 439 cm^{-1} has been tentatively assigned to the Ir–N bond. The Ir-PMO spectrum displayed the same vibrational modes described for the homogeneous analogue, along with characteristic Si–O (1101 cm^{-1}) and Si–C (1165 cm^{-1}) stretching vibrations. The solid-state UV-vis spectrum of Ir-PMO (Fig. 3d) revealed a slight red shift from 290 to 305 nm in the π–π* transitions due to the interaction between the iridium centres and the dppz units.[51] Two new absorption peaks centred at around 370 and 460 nm, also exhibited by the homogeneous counterpart, were attributed to metal–ligand charge transfer (MLCT) transitions.[52] Solid-state ^{13}C CP/MAS NMR also supported the incorporation of IrCp*Cl units on NdppzPMO (Fig. 3e). In addition to the typical resonances of NdppzPMO,[26] a new signal characteristic of Csp^2 from the Cp* ligand was observed at 91 ppm after the complexation of the iridium centre.[53] The expected ^{13}C chemical shift for the methyl groups in Cp* (–Cp($\underline{C}H_3$)$_5$) is ~9 ppm, which was likely masked by the intense signal from the ethylene-bridged groups of the PMO framework. The survey XPS spectrum of Ir-PMO exhibited binding signals in the Si 2p, O 1s, C 1s, N 1s, Cl 2p and Ir 4f regions (Fig. S14†). The N 1s spectrum was deconvoluted into two contributions ascribed to non-coordinated pyridine–pyridazine (399.6 eV) and a slightly upshifted Ir-coordinated N (400.3 eV) (Fig. S14d†). The Ir 4f spectrum revealed the presence of Ir $4f_{7/2}$ (62.4 eV) and Ir $4f_{5/2}$ (65.4 eV) spin–orbit components (Fig. 3f), which are consistent with those observed for the [IrCp*Cl(dppz)]Cl model complex, indicating the presence of the Ir^{III} oxidation state.[53,54]

The catalytic performance of Ir-PMO was evaluated at [CAN] : [Ir] = 1389 (3 mg Ir-PMO). Theoretically, a maximum of 250 μmol of oxygen can be evolved based on the stoichiometry of the reaction ($2H_2O + 4Ce^{IV} \rightarrow O_2 + 4H^+ + 4Ce^{III}$). Under these conditions, chemical water oxidation was catalysed by Ir-PMO with an initial TOF of 0.59 min^{-1} (Fig. 4a). The system evolved 210 μmol O_2 (84% O_2 yield) before plateauing at 28 h of reaction. At this point, CAN depletion was confirmed by the

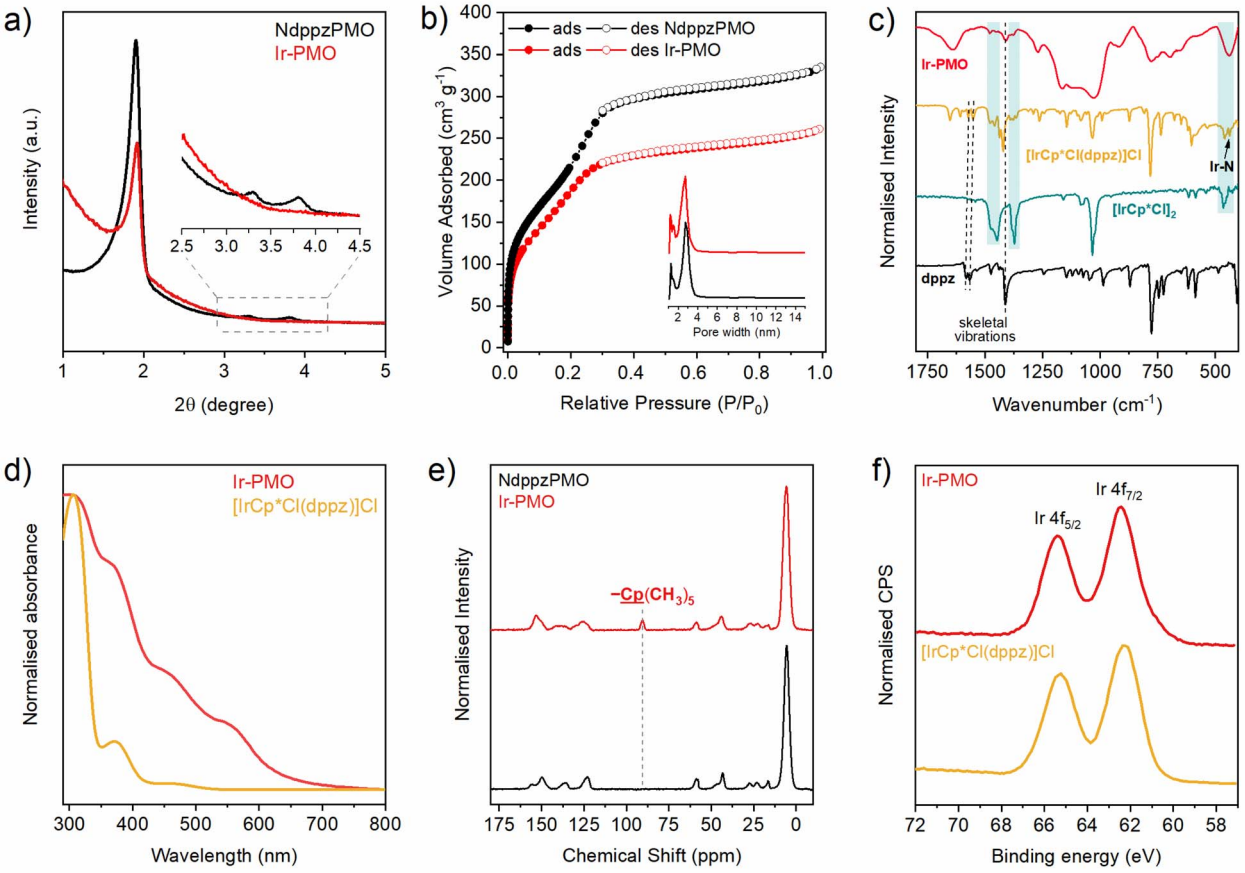

Fig. 3 (a) Low-angle PXRD of NdppzPMO and Ir-PMO. (b) Nitrogen adsorption–desorption isotherms and pore size distribution (inset) of NdppzPMO and Ir-PMO. (c) FT-IR spectra of [IrCp*Cl(dppz)]Cl and Ir-PMO. Characteristic vibrational modes of the dppz ligand and IrCp* moieties are indicated with dashed lines and blue shades, respectively. (d) UV-vis DRS spectra of Ir-PMO and UV-vis absorption spectra of [IrCp*Cl(dppz)]Cl (2.5×10^{-5} M) in MeCN. (e) ^{13}C CP/MAS NMR spectra of NdppzPMO and Ir-PMO. (f) High resolution Ir 4f XPS spectra of Ir-PMO and [IrCp*Cl(dppz)]Cl.

bleaching of the orange solution. The complete discoloration of the solution ruled out the presence of any oxidised (Ir^{IV} and Ir^{V}) or heterogeneous (IrO_x) species derived from the iridium complex, which would produce a blue-purple solution.[39,55,56] To further check the leaching of iridium species, the supernatant of the reaction was analysed by ICP, revealing a negligible concentration of iridium in the solution. Furthermore, a leaching test was carried out by filtration of the catalyst after 4 h of reaction (Fig. S15†). The filtrate produced a negligible additional amount of oxygen, demonstrating the heterogeneous nature of the catalysis.

To confirm the recyclability of the catalyst, Ir-PMO was recovered by vacuum filtration as a pale green solid, due to the presence of oxidised iridium species (Fig. S16b†). After washing with water and ethanol, the catalyst returned to its initial yellowish appearance, indicating the regeneration of the Ir^{III} species (Fig. S16a and c†). The catalyst was subsequently reused for five additional reaction cycles under identical conditions (Fig. 4a), showing consistent oxygen evolution yield till the 6th cycle (Table 1). This indicates excellent chemical stability and reusability of the heterogeneous catalyst. Interestingly, the oxygen evolution rates increased during the first three cycles, followed by a gradual drop in the activity during 4–6 cycles (Table 1). This indicates that the $[IrCp^*Cl(dppz)]^+$ species acts as a pre-catalyst and forms a more active catalyst, $[IrCp^*(OH_2)(dppz)]^{2+}$, during the water oxidation process. Similar results have been reported in the homogeneous phase, where reaction rates were faster as CAN was consumed, demonstrating the behaviour of Ir^{III} complexes as pre-catalysts.[15,57,58] Furthermore, the amount of oxygen evolved increased from 210 μmol in the 1st cycle to 220 and 228 μmol O_2 in the 2nd and 3rd catalytic cycles, respectively. This suggests that during the 1st cycle a fraction of CAN was consumed for catalyst activation, and it did not contribute to evolution of oxygen.[44,59,60] However, the initial TOFs decreased from the fourth run onwards, and a pronounced drop was observed for the 5th (0.5 min^{-1}) and the 6th cycle (0.25 min^{-1}), leading to a prolonged time until reaction completion. Overall, CAN-driven water oxidation catalysed by Ir-PMO resulted in evolution of a cumulative amount of 1349 μmol O_2 ($TON_{Ir} = 1874$) after six consecutive catalytic runs.

In comparison, the homogeneous [IrCp*Cl(dppz)]Cl complex produced O_2 with 91% yield and an initial TOF of

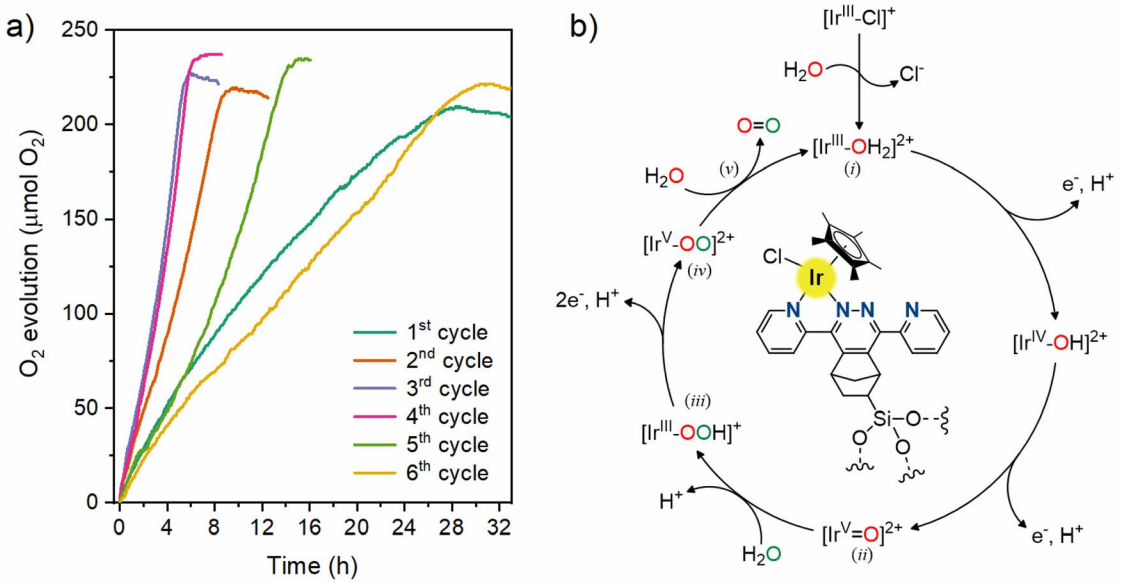

Fig. 4 (a) Time dependence oxygen evolution curves for Ir-PMO over six consecutive catalytic cycles. Experimental conditions: 100 mM CAN in HNO_3 (10 mL, 0.1 M, pH = 1) with Ir-PMO (3 mg, 0.72 μmol Ir). (b) Proposed mechanism for cerium-driven water oxidation by Ir-PMO.

2.36 min^{-1} under identical conditions, which is 4-fold higher than the initial rate observed for the heterogeneous system (0.59 min^{-1}). The faster rate in solution suggests that the diffusion of reactants and substrates through the mesopores of PMO is a limiting factor in the solid catalyst. However, the reaction rate of the homogeneous catalyst dropped dramatically to 1.09 min^{-1} during the second cycle, suggesting catalyst deactivation in solution (Fig. S17†). We hypothesise that it can be caused by dimerisation of the iridium complex once the bulky Cp* groups are oxidatively degraded, leading to competitive interaction rather than cooperativity for dinuclear iridium complexes in the WOR, similar to the behaviour observed by Crabtree *et al.*[61]

After the reaction, the Ir-PMO catalyst was characterised by PXRD, TEM, Raman spectroscopy, UV-vis DRS, and XPS. Although PXRD diffraction patterns exhibited a large decrease in the structural order (Fig. S18a†), TEM analysis corroborated the preservation of the initial ordered mesoporous structure even under the harsh reaction conditions together with the formation of CeO_2 nanoparticles on its surface (Fig. S19†). Although EDS elemental mapping confirmed the homogeneous distribution of Ir (Fig. S20†), the Fast Fourier Transform (FFT) pattern analysis of the resulting particles corroborated the deposition of cerium oxide (CeO_2) nanoparticles on the sample. The formation of surface cerium oxide nanoparticles was further confirmed by Raman spectroscopy (Fig. S18b†), displaying the triply degenerate (F2g) mode of symmetric Ce–O stretching vibration at 454 cm^{-1} and a small shoulder centred at ~610 cm^{-1} due to the presence of oxygen vacancies (D). Since the Ce–O vibration mode is highly sensitive to oxygen related disorder in the CeO_2 structure, the broadness of this peak is further evidence of the formation of small-sized particles.[60] The UV-vis diffuse reflectance spectrum of the heterogeneous catalyst after six catalytic cycles showed extended absorption in the UV range due to the deposition of CeO_2 nanoparticles and an additional broad band (600–800 nm) that might be associated with oxidised Ir^{IV} species (Fig. S18c†).[38,62] Furthermore, characteristic MLCT transitions disappeared after the WOR, which is in line with the reaction mechanism and the oxidative degradation reported for the Cp* ligand.[18,22,25] Cp* degradation of the heterogeneous $[IrCp^*Cl(dppz)]^+$ sites was confirmed by ^1H qNMR of the WOR supernatant (Fig. S21†), confirming the appearance of 2 μmol acetic acid, corresponding to 2.7 times the initial Cp* ligands, along with a residual amount of formic acid (0.1 μmol). Interestingly, no downfield signals associated with aromatic protons from the dppz ligand were observed, indicating strong anchoring of the Ndppz groups to the PMO scaffold even under strongly acidic conditions. XPS of the post-catalysis material showed the presence of surface ammonium (403.4 eV) and nitrate species (407.2 eV) due to the use of CAN as a sacrificial oxidant (Fig. S22a†).[22,63] The activation of the iridium sites through Cl^- substitution was confirmed by the absence of Cl 2p electronic transitions (Fig. S22b†). The Ir 4f XPS spectrum confirmed that the electronic structure of the Ir^{III} catalytic centres remained largely unaffected after the catalytic run (Fig. S22c†). To avoid partial reduction of Ce species, short exposure X-ray analysis was conducted for the Ce 3d region (Fig. S22d†). Cerium 3d core-level XPS spectra displayed characteristic Ce^{IV} spin–orbit doublets: ν–u ($3d_{5/2}$–$3d_{3/2}$, 882.8 and 901.2 eV), ν″–u″ (888.1 and 907.6 eV), and ν‴–u‴ (898.4 and 916.9 eV).[64]

To demonstrate the impact of the PMO scaffold, the catalytic performance of Ir-PMO was compared with that of a [IrCp*Cl(dppz)]Cl complex immobilised on SBA-15 mesoporous silica (Ir content: 0.142 mmol Ir per g), hereafter denoted as Ir-SBA.[51] Although Ir-SBA displays a larger pore size (7.1 nm), which is approximately 2.6-fold larger than that of

Ir-PMO, the specific surface area was significantly lower (383 m^2 g^{-1}). Therefore, the surface concentration of active sites (μmol Ir per m^2) is comparable for both, being 0.39 and 0.37 μmol Ir per m^2 for Ir-PMO and Ir-SBA, respectively, indicating a similar distribution of iridium complexes per unit area. Since heterogeneous catalysis in mesoporous supports largely depends on the efficient diffusion of chemicals within the pores, the variations in the pore size diameter are deemed to be important for benchmarking the activity. Time dependent oxygen evolution kinetics over six catalytic cycles for Ir-SBA are shown in Fig. S23 and S24,† whereas catalyst metrics are summarised in Table S8.† Additionally, the cumulative amounts of oxygen evolved by Ir-PMO and Ir-SBA over six cycles are shown in Fig. S25,† revealing an initial activation period. Ir-SBA showed a higher initial oxygen evolution rate compared to Ir-PMO (0.72 *vs.* 0.59 min^{-1}) during the first run. Interestingly, Ir-SBA displayed a steady decrease in TOF over successive recycling runs, which indicates that all the catalytic sites were activated during the first water oxidation cycle. Indeed, this fact is further supported by the lower oxygen yield obtained for Ir-SBA (78 *vs.* 84%), indicating a higher CAN consumption for oxidative activation of the pre-catalyst. The superior TOF value shown by Ir-SBA for the first run can be attributed to the larger pore size of the SBA scaffold that allowed greater access to the Ir centres. In contrast, the oxygen evolution rate for Ir-PMO became faster than that of Ir-SBA in the subsequent catalytic cycles (2^{nd} to 4^{th}). After the initial activation period during the first cycle, steady oxygen evolution rates were observed for both catalysts during the next four cycles (2^{nd} to 4^{th} cycles) with clearly faster reaction kinetics for Ir-PMO (Fig. S25†). Overall, Ir-PMO produced 1349 μmol oxygen in 110 hours with a ~90% yield, while Ir-SBA evolved 1315 μmol oxygen in 160 hours with ~88% yield. This data demonstrate the robustness of both catalysts with >4 days of operation and a slightly superior performance of Ir-PMO. We hypothesise that the bridging ethylene groups in PMO renders its pores hydrophobic, which facilitates the diffusion of sacrificial oxidant through the channels to the iridium active sites.[65–68] Furthermore, the differences in catalytic performance for both heterogeneous catalysts, linked to diffusion limitations, support the hypothesis that water oxidation catalysis mainly occurs within the pores. Similar to Ir-PMO, the performance of Ir-SBA in cerium-driven water oxidation declined substantially after six catalytic cycles. This phenomenon could be attributed to a progressive blockage of the pores due to the deposition of cerium oxide (CeO_2), which is particularly pronounced in Ir-PMO due to the smaller pore dimensions. Similar results have also been reported previously by Inagaki *et al.*,[25] who observed a large decrease in the structural order and a significant drop in the BET surface area after using an IrCp*Cl functionalised bipyridine-PMO for three catalytic cycles.

Based on previous studies,[15,29,35,59,69] we propose a tentative mechanism for the cerium-driven water oxidation in Fig. 4b. The proposed mechanism involves the transfer of multiple electrons for the generation of the key active intermediate for catalysis and O–O bond formation through the reaction of the Ir^V oxo intermediate. At the outset, an Ir^{III} aqua complex (i) is obtained through the replacement of the Cl^- ligand from the $[IrCp^*Cl(dppz)]^+$ pre-catalyst with a molecule of H_2O. This catalyst undergoes oxidative activation *via* two proton-coupled electron transfer (PCET) processes facilitated by Ce^{IV} to form the transient $Ir^V{=}O$ species (ii). Considering the isolated nature of the catalytic centres and their homogeneous distribution throughout the PMO framework, which ensures a low local catalyst concentration to prevent the intermolecular coupling mechanism (I2M), we hypothesise a heterogeneous water oxidation mechanism based on a water nucleophilic attack (WNA). Furthermore, this mechanistic pathway is particularly relevant in the context of IrCp*-catalysed water oxidation.[14,35,70] The $Ir^V{=}O$ intermediate undergoes a water nucleophilic attack with the concomitant formation of the O–O bond through a hydroperoxo intermediate (iii), which is further oxidized to form a superoxo species (iv). Lastly, oxygen is released through the reduction of the iridium centre to Ir^{III} and the coordination of a water molecule (v), thus regenerating the catalyst.

3. Conclusions

We report synthesis and characterisation of a novel $[IrCp^*Cl(dppz)]^+$ water oxidation complex and its subsequent immobilisation on a PMO scaffold to synthesize a heterogeneous catalyst. UV-vis and DLS experiments demonstrated the molecular nature of the catalysis for the half-sandwich Ir^{III} complex. The iridium complex was immobilised onto a PMO scaffold *via* coordination to the surface-bound dppz ligands to construct a heterogeneous catalyst with molecular active sites, thus highlighting the versatility of NdppzPMO as a chelating platform. While the homogeneous catalyst suffers from catalyst deactivation under strong oxidising conditions, the heterogenisation of the active sites provides enhanced stability and extends the catalyst lifetime, demonstrating efficient performance for cerium-driven water oxidation with a cumulative generation of 1349 μmol O_2 (TON = 1874 *vs.* [Ir]). However, the Cp* ligand remained susceptible to oxidative degradation pathways. The absence of leached species highlighted the robustness of Ir-PMO assembly. We speculate that the deactivation of the system is caused by pore blockage from deposition of cerium oxide nanoparticles. A comparison of the catalytic activity with an analogous iridium complex grafted onto mesoporous silica (SBA-15) showed that Ir-PMO outperforms Ir-SBA-15 catalyst. We hypothesise that the higher hydrophobicity of the surface of Ir-PMO facilitates diffusion of the sacrificial oxidant within the pores. These findings emphasise the importance of tuning the hydrophobic/hydrophilic ratio to tailor PMOs for specific applications such as chemical-driven water oxidation.

4. Experimental section

4.1. Synthesis of materials

Synthesis of [IrCp*Cl(dppz)]Cl. 3,6-Dipyridin-2-ylpyridazine was synthesised as previously reported.[71] For the [IrCp*Cl(dppz)]Cl complex, a solution of dppz (63.5 mg,

0.27 mmol, 2.5 equiv.) in DCM (2.5 mL) was added to a solution of $[IrCp^*Cl_2]_2$ (87 mg, 0.11 mmol, 1 equiv.) in DCM (7.5 mL). After stirring for 2.5 h at room temperature, 25 mL of diethyl ether was added to the reaction mixture. The resulting yellow precipitate was collected by filtration, washed with diethyl ether and dried under vacuum. The yield was 137.5 mg (79%). Yellow crystals suitable for X-ray diffraction were obtained by slow evaporation of an acetonitrile solution of the complex at room temperature. ^{1}H NMR (CD_3CN): δ (ppm) = 9.02 (d, J = 9.0 Hz, 1H, Ar H), 8.98 (ddd, J = 5.6, 1.5, 0.7 Hz, 1H, Ar H), 8.85 (ddd, J = 4.8, 1.8, 0.9 Hz, 1H, Ar H), 8.82 (d, J = 8.8 Hz, 1H, Ar H), 8.61 (dt, J = 8.0, 1.0 Hz, 1H, Ar H), 8.58 (d, J = 8.1 Hz, 1H, Ar H), 8.30 (td, J = 7.9, 1.4 Hz, 1H, Ar H), 8.10 (td, J = 7.8, 1.7 Hz, 1H), 7.89 (ddd, J = 7.7, 5.6, 1.4 Hz, 1H, Ar H), 7.64 (ddd, J = 7.6, 4.7, 1.1 Hz, 1H, Ar H), 1.75 (s, 15H, Cp*) (Fig. S26†). ^{13}C NMR (CD_3CN): δ (ppm) = 162.05, 159.25, 153.61, 152.58, 151.33, 151.02, 140.95, 138.72, 130.42, 130.37, 128.62, 127.05, 126.05, 122.59, 91.32, 8.54 (Fig. S27†). UV-vis, λ_{max}, nm (ε, M^{-1} cm^{-1}): 306 (27 026 M^{-1} cm^{-1}), 370 (shoulder, 4526 M^{-1} cm^{-1}), 455 (weak shoulder, 601 M^{-1} cm^{-1}). ESI-MS (positive mode): $[M - 1Cl^-]^+$ = 597.1384 (597.1397), $[M - 2Cl^-]^{2+}$ = 281.0858 (281.0855).

Synthesis of Ir-PMO. NdppzPMO was obtained following the synthetic procedure described in a previous report (N content: 2.25 wt%, ~0.4 mmol dppz per g).[26] The iridium catalyst was prepared by postsynthetic metalation of the as-synthesised NdppzPMO. A suspension of NdppzPMO (100 mg) and $[IrCp^*Cl_2]_2$ (0.02 mmol, 17 mg) in dry ethanol (30 mL) was stirred overnight under reflux. The resulting solid was filtered and washed with ethanol and dichloromethane to yield Ir-PMO as a pale orange powder (Ir content: 0.24 mmol Ir per g).

4.2. Water oxidation experiments

In a typical heterogeneous cerium-driven water oxidation reaction, a two-neck round-bottom flask connected to a switchable three-way valve through a Torion screw was charged with Ir-PMO (3 mg, 0.72 μmol Ir). The glass reactor was then sealed with a rubber septum and purged under an inert gas atmosphere by performing three vacuum/nitrogen cycles. In a separate vessel, 1.4 g CAN (2.5 mmol) was dissolved in 25 mL of HNO_3 solution (0.1 M, pH = 1) and subsequently purged with a gentle nitrogen flow for 10 min. The degassed CAN solution (10 mL) was injected into the reactor and maintained at 25 °C with stirring. For homogeneous catalysis, water oxidation was initiated by injecting a degassed stock solution of the [IrCp*Cl(dppz)]Cl complex in HNO_3 (pH 0.1 M, pH = 1). The amount of oxygen evolved was measured by using a pressure transductor (Man on the Moon series X103) through monitoring the data acquisition at regular 5 min intervals.

Upon completion of the reaction, the suspension was filtered under reduced pressure and washed with deionised water and ethanol. The recovered catalyst was vacuum dried before being reused under identical reaction conditions.

Catalyst metrics are indicated by the initial oxygen evolution rates in terms of turnover frequency (TOF, mol O_2 evolved per mole of active site per unit time) during the first 15 minutes following the addition of the sacrificial oxidant and the turnover number (TON, mol O_2 evolved per mole of active site).

Data availability

The data supporting this article have been included as part of the ESI.† The crystallographic data for [IrCp*Cl(dppz)]Cl have been deposited at CCDC under deposition number 2404149.

Conflicts of interest

There are no conflicts to declare.

Acknowledgements

The authors wish to acknowledge the financial support from the Andalusian Regional Government (Project ProyExcel_00492 and FQM-346 group), FEDER Funds, and projects (PID2022/142657OB-I00/MCIN/AEI/10.13039/501100011033/FEDER, UE and PDC2022-133973-I00/AEI/10.13039/501100011033 Mecanismo de Recuperación y Resiliencia de la Unión Europea-Next Generation EU), and the Royal Society International Exchange Grant (IES/R1/231335). R. R. L. acknowledges the Ramón Areces Foundation for the postdoctoral research fellowship [BEVP36S17981]. J. A.-G. would like to acknowledge the "Juan de la Cierva" fellowship (JDC 2022-048903-I), funded by MCIN/AEI/10.13039/501100011033 and the European Union "NextGenerationEU"/PRTR". Dr Miguel Castillo-Rodríguez is also acknowledged for assisting with TEM measurements. The authors are thankful to the staff at the Central Service for Research Support (SCAI) of the University of Córdoba for their assistance in ICP-MS measurements. The authors acknowledge JBL Science facilities at the University of Lincoln (Joseph Banks Laboratories), UK, for the structural characterization (HRMS) of the target compounds.

References

1 M. G. Walter, E. L. Warren, J. R. McKone, S. W. Boettcher, Q. Mi, E. A. Santori and N. S. Lewis, *Chem. Rev.*, 2010, **110**, 6446–6473.
2 A. Zouni, H.-T. Witt, J. Kern, P. Fromme, N. Krauss, W. Saenger and P. Orth, *Nature*, 2001, **409**, 739–743.
3 S. Ye, C. Ding, M. Liu, A. Wang, Q. Huang and C. Li, *Adv. Mater.*, 2019, **31**, 1902069.
4 R. Matheu, P. Garrido-Barros, M. Gil-Sepulcre, M. Z. Ertem, X. Sala, C. Gimbert-Suriñach and A. Llobet, *Nat. Rev. Chem*, 2019, **3**, 331–341.
5 M. Yagi and M. Kaneko, *Chem. Rev.*, 2001, **101**, 21–36.
6 J. Li, C. A. Triana, W. Wan, D. P. Adiyeri Saseendran, Y. Zhao, S. E. Balaghi, S. Heidari and G. R. Patzke, *Chem. Soc. Rev.*, 2021, **50**, 2444–2485.
7 H. Zhang, W. Tian, X. Duan, H. Sun, S. Liu and S. Wang, *Adv. Mater.*, 2020, **32**, 1904037.
8 R. Cao, W. Lai and P. Du, *Energy Environ. Sci.*, 2012, **5**, 8134.
9 R. Lalrempuia, N. D. McDaniel, H. Müller-Bunz, S. Bernhard and M. Albrecht, *Angew. Chem., Int. Ed.*, 2010, **49**, 9765–9768.

10 A. Savini, G. Bellachioma, G. Ciancaleoni, C. Zuccaccia, D. Zuccaccia and A. Macchioni, *Chem. Commun.*, 2010, **46**, 9218.
11 A. Bucci, A. Savini, L. Rocchigiani, C. Zuccaccia, S. Rizzato, A. Albinati, A. Llobet and A. Macchioni, *Organometallics*, 2012, **31**, 8071–8074.
12 A. Savini, A. Bucci, G. Bellachioma, S. Giancola, F. Palomba, L. Rocchigiani, A. Rossi, M. Suriani, C. Zuccaccia and A. Macchioni, *J. Organomet. Chem.*, 2014, **771**, 24–32.
13 M. Li, K. Takada, J. I. Goldsmith and S. Bernhard, *Inorg. Chem.*, 2016, **55**, 518–526.
14 J. F. Hull, D. Balcells, J. D. Blakemore, C. D. Incarvito, O. Eisenstein, G. W. Brudvig and R. H. Crabtree, *J. Am. Chem. Soc.*, 2009, **131**, 8730–8731.
15 J. M. Thomsen, D. L. Huang, R. H. Crabtree and G. W. Brudvig, *Dalton Trans.*, 2015, **44**, 12452–12472.
16 T. J. Meyer, M. V. Sheridan and B. D. Sherman, *Chem. Soc. Rev.*, 2017, **46**, 6148–6169.
17 J. Li, R. Güttinger, R. Moré, F. Song, W. Wan and G. R. Patzke, *Chem. Soc. Rev.*, 2017, **46**, 6124–6147.
18 A. Macchioni, *Eur. J. Inorg. Chem.*, 2019, **2019**, 7–17.
19 A. K. Singh and L. Roy, *ACS Omega*, 2024, **9**, 9886–9920.
20 I. Corbucci, A. Macchioni and M. Albrecht, in *Iridium(III) in Optoelectronic and Photonics Applications*, Wiley, 2017, pp. 617–654.
21 C. Wang, Z. Xie, K. E. DeKrafft and W. Lin, *J. Am. Chem. Soc.*, 2011, **133**, 13445–13454.
22 C. Wang, J.-L. Wang and W. Lin, *J. Am. Chem. Soc.*, 2012, **134**, 19895–19908.
23 X. Liu, Y. Goto, Y. Maegawa, T. Ohsuna and S. Inagaki, *APL Mater.*, 2014, **2**, 113308.
24 P. Van Der Voort, D. Esquivel, E. De Canck, F. Goethals, I. Van Driessche and F. J. Romero-Salguero, *Chem. Soc. Rev.*, 2013, **42**, 3913–3955.
25 X. Liu, Y. Maegawa, Y. Goto, K. Hara and S. Inagaki, *Angew. Chem., Int. Ed.*, 2016, **55**, 7943–7947.
26 R. Rojas-Luna, M. Castillo-Rodríguez, J. R. Ruiz, C. Jiménez-Sanchidrián, D. Esquivel and F. J. Romero-Salguero, *Dalton Trans.*, 2022, **51**, 18708–18721.
27 M.-T. Youinou and R. Ziessel, *J. Organomet. Chem.*, 1989, **363**, 197–208.
28 L. Tong, A. K. Inge, L. Duan, L. Wang, X. Zou and L. Sun, *Inorg. Chem.*, 2013, **52**, 2505–2518.
29 K. S. Joya, N. K. Subbaiyan, F. D'Souza and H. J. M. de Groot, *Angew. Chem., Int. Ed.*, 2012, **51**, 9601–9605.
30 N. D. McDaniel, F. J. Coughlin, L. L. Tinker and S. Bernhard, *J. Am. Chem. Soc.*, 2008, **130**, 210–217.
31 D. C. Marelius, S. Bhagan, D. J. Charboneau, K. M. Schroeder, J. M. Kamdar, A. R. McGettigan, B. J. Freeman, C. E. Moore, A. L. Rheingold, A. L. Cooksy, D. K. Smith, J. J. Paul, E. T. Papish and D. B. Grotjahn, *Eur. J. Inorg. Chem.*, 2014, **2014**, 676–689.
32 A. R. Parent, R. H. Crabtree and G. W. Brudvig, *Chem. Soc. Rev.*, 2013, **42**, 2247–2252.
33 A. Bucci, G. Menendez Rodriguez, G. Bellachioma, C. Zuccaccia, A. Poater, L. Cavallo and A. Macchioni, *ACS Catal.*, 2016, **6**, 4559–4563.
34 G. Menendez Rodriguez, A. Bucci, R. Hutchinson, G. Bellachioma, C. Zuccaccia, S. Giovagnoli, H. Idriss and A. Macchioni, *ACS Energy Lett.*, 2017, **2**, 105–110.
35 J. D. Blakemore, N. D. Schley, D. Balcells, J. F. Hull, G. W. Olack, C. D. Incarvito, O. Eisenstein, G. W. Brudvig and R. H. Crabtree, *J. Am. Chem. Soc.*, 2010, **132**, 16017–16029.
36 A. R. Parent, T. P. Brewster, W. De Wolf, R. H. Crabtree and G. W. Brudvig, *Inorg. Chem.*, 2012, **51**, 6147–6152.
37 A. Savini, A. Bucci, G. Bellachioma, L. Rocchigiani, C. Zuccaccia, A. Llobet and A. Macchioni, *Eur. J. Inorg. Chem.*, 2014, **2014**, 690–697.
38 U. Hintermair, S. M. Hashmi, M. Elimelech and R. H. Crabtree, *J. Am. Chem. Soc.*, 2012, **134**, 9785–9795.
39 U. Hintermair, S. W. Sheehan, A. R. Parent, D. H. Ess, D. T. Richens, P. H. Vaccaro, G. W. Brudvig and R. H. Crabtree, *J. Am. Chem. Soc.*, 2013, **135**, 10837–10851.
40 L. S. Sharninghausen, S. B. Sinha, D. Y. Shopov, B. Choi, B. Q. Mercado, X. Roy, D. Balcells, G. W. Brudvig and R. H. Crabtree, *J. Am. Chem. Soc.*, 2016, **138**, 15917–15926.
41 T. K. Michaelos, D. Y. Shopov, S. B. Sinha, L. S. Sharninghausen, K. J. Fisher, H. M. C. Lant, R. H. Crabtree and G. W. Brudvig, *Acc. Chem. Res.*, 2017, **50**, 952–959.
42 B. Mahanti, G. González Miera, E. Martínez-Castro, M. Bedin, B. Martín-Matute, S. Ott and A. Thapper, *ChemSusChem*, 2017, **10**, 4616–4623.
43 R. Puerta-Oteo, M. V. Jiménez and J. J. Pérez-Torrente, *Catal. Sci. Technol.*, 2019, **9**, 1437–1450.
44 Z. Mazloomi, J. Margalef, M. Gil-Sepulcre, N. Romero, M. Albrecht, A. Llobet, X. Sala, O. Pàmies and M. Diéguez, *Inorg. Chem.*, 2020, **59**, 12337–12347.
45 D. Lionetti, V. W. Day and J. D. Blakemore, *Organometallics*, 2017, **36**, 1897–1905.
46 M. Ladwig and W. Kaim, *J. Organomet. Chem.*, 1992, **439**, 79–90.
47 T. P. Brewster, J. D. Blakemore, N. D. Schley, C. D. Incarvito, N. Hazari, G. W. Brudvig and R. H. Crabtree, *Organometallics*, 2011, **30**, 965–973.
48 G. Luciani, C. Decavoli, R. H. Crabtree and G. W. Brudvig, *Energy Fuels*, 2025, **39**, 6549–6558.
49 R. Rojas-Luna, F. J. Romero-Salguero, D. Esquivel and S. Roy, *ACS Appl. Energy Mater.*, 2024, **7**, 5924–5936.
50 L. Ye and Z. Yao, *Appl. Organomet. Chem.*, 2024, **38**, e7642.
51 R. Rojas-Luna, J. Amaro-Gahete, C. Jiménez-Sanchidrián, J. R. Ruiz, D. Esquivel and F. J. Romero-Salguero, *Inorg. Chem.*, 2023, **62**, 11954–11965.
52 S. Zhang, H. Wang, M. Li, J. Han, X. Liu and J. Gong, *Chem. Sci.*, 2017, **8**, 4489–4496.
53 S. De, L. Gevers, A.-H. Emwas and J. Gascon, *ACS Sustain. Chem. Eng.*, 2019, **7**, 3933–3939.
54 A. V. Bavykina, M. G. Goesten, F. Kapteijn, M. Makkee and J. Gascon, *ChemSusChem*, 2015, **8**, 809–812.
55 S. E. Castillo-Blum, D. T. Richens and A. G. Sykes, *Inorg. Chem.*, 1989, **28**, 954–960.
56 J. D. Blakemore, N. D. Schley, G. W. Olack, C. D. Incarvito, G. W. Brudvig and R. H. Crabtree, *Chem. Sci.*, 2011, **2**, 94–98.

57 D. Hong, M. Murakami, Y. Yamada and S. Fukuzumi, *Energy Environ. Sci.*, 2012, **5**, 5708–5716.
58 D. B. Grotjahn, D. B. Brown, J. K. Martin, D. C. Marelius, M.-C. Abadjian, H. N. Tran, G. Kalyuzhny, K. S. Vecchio, Z. G. Specht, S. A. Cortes-Llamas, V. Miranda-Soto, C. van Niekerk, C. E. Moore and A. L. Rheingold, *J. Am. Chem. Soc.*, 2011, **133**, 19024–19027.
59 A. Savini, P. Belanzoni, G. Bellachioma, C. Zuccaccia, D. Zuccaccia and A. Macchioni, *Green Chem.*, 2011, **13**, 3360–3374.
60 J. A. Woods, R. Lalrempuia, A. Petronilho, N. D. McDaniel, H. Müller-Bunz, M. Albrecht and S. Bernhard, *Energy Environ. Sci.*, 2014, **7**, 2316–2328.
61 J. Graeupner, U. Hintermair, D. L. Huang, J. M. Thomsen, M. Takase, J. Campos, S. M. Hashmi, M. Elimelech, G. W. Brudvig and R. H. Crabtree, *Organometallics*, 2013, **32**, 5384–5390.
62 G. Jayakumar, A. Albert Irudayaraj and A. Dhayal Raj, *Opt. Quantum Electron.*, 2019, **51**, 312.
63 L. S. Kasten, J. T. Grant, N. Grebasch, N. Voevodin, F. E. Arnold and M. S. Donley, *Surf. Coat. Technol.*, 2001, **140**, 11–15.
64 J. Yang, Y. Jia, B. Huang, X. Li, L. Guo, A. Zheng, R. Luque and Y. Sun, *ACS Sustain. Chem. Eng.*, 2020, **8**, 6371–6380.
65 H. Li, F. Zhang, Y. Wan and Y. Lu, *J. Phys. Chem. B*, 2006, **110**, 22942–22946.
66 Y. Wan, D. Zhang, Y. Zhai, C. Feng, J. Chen and H. Li, *Chem.–Asian J.*, 2007, **2**, 875–881.
67 H. Li, H. Yin, F. Zhang, H. Li, Y. Huo and Y. Lu, *Environ. Sci. Technol.*, 2009, **43**, 188–194.
68 M. Shimizu, K. Michikawa, Y. Maegawa, S. Inagaki and K. Fujita, *ACS Appl. Nano Mater.*, 2020, **3**, 2527–2535.
69 D. R. Weinberg, C. J. Gagliardi, J. F. Hull, C. F. Murphy, C. A. Kent, B. C. Westlake, A. Paul, D. H. Ess, D. G. McCafferty and T. J. Meyer, *Chem. Rev.*, 2012, **112**, 4016–4093.
70 D. G. H. Hetterscheid and J. N. H. Reek, *Chem. Commun.*, 2011, **47**, 2712.
71 H. Bakkali, C. Marie, A. Ly, C. Thobie-Gautier, J. Graton, M. Pipelier, S. Sengmany, E. Léonel, J. Y. Nédélec, M. Evain and D. Dubreuil, *Eur. J. Org Chem.*, 2008, **2008**, 2156–2166.